

A deep artificial neural network assisted genetic algorithm method to optimize a slotted hydrofoil

Mahya Hajihassanpour¹

Jacobs, Leeds, UK

Abstract

Slotting a hydrofoil is an effective way to passively control the cavitating flow to reduce the cavity pocket size leading to a reduction in vibration, noise, and erosion. However, this comes with losses in the hydrodynamic performance of the hydrofoil including its lift coefficient. To avoid this as much as possible, optimizing the slotted hydrofoil in terms of the location and the angle is of prime importance. The optimization is achieved by designing a deep Artificial Neural Network (ANN) to act as a surrogate model in the process of the genetic algorithm. The training dataset in deep ANN is gathered through simulations that are based on a newly developed Frink finite volume solver for the preconditioned Euler equations. Results obtained indicate that this optimization approach is effective such that the cavity pocket size can be shrieked by about 60 % with a penalty of about 10 % reduction in the hydrofoil's lift coefficient.

Keywords

Optimized slotted hydrofoil, Deep Artificial Neural Network (ANN), Genetic algorithm, Surrogate model, Frink finite volume method, Cavitating flow

¹ mahya.hajihassanpour@jacobs.com

1. Introduction

Cavitating flows are widely seen in many practical applications such as in pumps, pipes, hydro turbines, and blood vessels, or on watercraft including ships, boats, amphibious, submarines, and hovercraft. Cavitation takes place when the liquid is accelerated and consequently the local pressure becomes lower than the vapor pressure. In such a condition, the preexisted vapor nucleus will grow in the liquid medium and eventually create a cavity pocket filled with both liquid and many vapor nucleus. When these nuclei arrive at places with higher pressures, condensation occurs. In the condensation process, the nucleus violently collapses and high-pressure waves will be generated that cause erosion, annoying sounds, and vibration that may cause a shorter lifetime for the product [1]. Flow control techniques can be used to avoid these.

Flow control techniques can be categorized into passive and active methods. In the case of active flow control, different methods such as the injection [2]–[5] or suction [6] are employed. As for the passive control methods vortex generators [7], [8], leading-edge slats [9], leading-edge serration [10], slotted hydrofoils [11]–[15], micro-cylinders [16], hydrofoils with cavity [17], roughness [18], and flexible hydrofoil [19] have been used. Owing to the simplicity and economic efficiency of passive control methods over the active ones, formers are more applied to practical applications. Here, the passive flow control of the slotted hydrofoil is utilized.

A few studies about the slotted hydrofoil have been performed in the literature [11]–[15]. The idea of using slotted hydrofoils comes from the work of Capurso et al. [11], [12] where three slots located near the leading-edge of the NACA 0009 hydrofoil have been considered. Their results show a 93% reduction for the total length of the cavity, but a 25% reduction in the lift coefficient. The optimization has not been performed by them. Conesa and Liem [13], [14] have studied the effect of the entry and exit widths of the slot and its angle on the performance of the Clark-Y hydrofoil, but they have fixed the slot location near the leading-edge in the optimization process. Their study shows that the optimized slotted hydrofoil can achieve higher performance with a 50% reduction in cavity pocket in comparison with the base hydrofoil. An experimental and numerical study has been done by Ni et al. [15] to investigate the performance of a slotted hydrofoil operating close to a free surface. The slotted hydrofoil is constructed from the base hydrofoil NACA 634-021. No optimization has been performed, and the slotted hydrofoil had a better performance in comparison with the base hydrofoil. Here, the optimization is done by changing

the location and the angle of the slot on the NACA 66 (MOD) base hydrofoil as it is widely used in many practical real-world artifacts.

Nowadays, multi-objective optimizations are frequently used to design engineering artifacts. The solution to these complex design optimization problems, such as the problem that is addressed in this paper, are generally computationally expensive. To reduce the computational costs, surrogate model approximations are intensively used in the literature [20], [21]. surrogate models use limited combinations of inputs (sample points) and outputs to provide a mapping from the input space to the output space which essentially reduces the computational cost [22], [23]. surrogate models come in several forms. Surrogate models can be either deterministic or stochastic, low-order or high-order polynomial regression models, discrete or continuous, and local or global. Some of the better-known surrogate models are the Multivariate Adaptive Regression Splines, Radial Basis Function, Polynomial Regression, Neural Networks, Kriging, etc. [20]. The advantages or disadvantages of surrogate models vary case by case and we cannot easily say essentially one of them is better than the others, and an extensive study is needed between surrogate models to judge their priority, which is beyond the scope of this paper. In the current study, a deep Artificial Neural Network (ANN) is employed. Choosing the sample training data points is of paramount importance to have an accurate surrogate model that both represents the design space adequately and does not encounter any numerical difficulties. Usually, to determine the sample points the theory of the Design of Experiments (DoE) is employed. Several used DoE methods are the factorial, central decomposition, alphabetical optimal, and Box-Behnken methods [24], [25]. These methods usually tend to push the sample points towards the boundaries of the design space. More recent methods address this problem and try to uniformly distribute the sample points within the boundaries. To name a few, Maximum Entropy, MiniMax, Orthogonal Arrays, and Latin Hypercube algorithms can be mentioned [20], [21], [24]. Latin Hypercube Sampling (LHS) is a straightforward well-established sampling method in the literature that is chosen to be used in this research. In LHS an even random sampling is employed and then all the chosen variables are randomly combined to give the samples required.

While the surrogate models together with DoE methods are used to find out the optimization functions defined in the design space, the optimizers are required to figure out where minimums occur. The optimizers can be categorized into two gradient-based and gradient-free

groups [26]. As the name suggests, a gradient-based optimizer uses the gradient of the objective function to find the optimum solution. This dependence on the gradient raises two main issues. First, to use a gradient-based optimizer the gradient of the function must be either known analytically or computed numerically. This increases the computational cost. Second, and more importantly, a gradient-based optimizer can get stuck in a local optimum. On the other hand, a gradient-free/heuristic/Metaheuristics optimizer uses a random operator to search the design space. Decades of research resulted in the development of many Metaheuristics. To name a few well-known metaheuristics, we may mention Particle Swarm Optimization (PSO), Differential Evolution (DE), Genetic Algorithms (GA), and Ant Colony Optimization (ACO) [27]. Inspired by Darwin's natural evolution theory, the GA mimics the natural evolution to find the optimal solution [26]–[28]. Within the GA, the design parameters are interpreted as characteristics of individuals. Taking all individuals among a population, the solutions evolve through cross-over, mutation, and elitism operators to find the optimum. The random operator helps the Genetic Algorithm to explore the design space better, and the gradient-independence empowers it to deal with any kind of objective function. This rigorous searching capability grants the metaheuristics and the GA particularly the name “global optimization methods” [26] and it is used here.

Realizations are needed to create a surrogate model (also called a surrogate model). Cavitating flow realizations are usually achieved by simulating inviscid, laminar, or turbulent fluid flows. Assuming water as the main medium, the Reynolds number is often high in real applications so that the laminar cavitating flow can be only seen seldom, however, the inviscid flow condition can provide acceptable results and the turbulent flow simulations are usually expensive. The pressure distribution over the hydrofoil determines the cavity pocket size and the lift coefficient can be reasonably captured by the solution of inviscid Euler equations. In an inviscid flow simulation, a fewer number of grid points in comparison with turbulent flows are required in simulations and then the computational cost can be dramatically decreased. Therefore, the preconditioned Euler equations representing inviscid flows are used here.

The preconditioned Euler equations should be solved using an appropriate numerical method. Different methods have been utilized in the literature for solving these governing equations, such as the central finite difference [29], compact [30], central finite volume [31], Quadratic Upstream Interpolation for the Convective Kinematics (QUICK) [32], weighted

essentially non-oscillating (WENO) [33], immersed boundary [34], upstream finite element [35], and discontinuous Galerkin [36]–[38] methods. Here, the Frink numerical method [39] is applied to discretize the governing equation, and an appropriate artificial dissipation term, based on the one proposed by Jameson et al. [40], is added for suppressing artificial oscillations in the solution domain and to provide a stable, accurate, and reasonably fast solver.

In this paper, the algorithm of the optimizer is given in Section 2. The design of the deep ANN is described in Section 3 and the details of the newly Frink finite volume-based simulator is given in Section 4. Results obtain are discussed in Section 5 and the paper is ended up through a conclusion in Section 6.

2. Optimizer

The optimization parameters are the slot angle θ and its location x_{slot} with constraints of $0^\circ \leq \theta \leq 85^\circ$ and $0 \leq x_{slot} \leq 0.4$. The optimization parameters are geometrically introduced in Fig. 1. As shown, the slot location varies from the middle chord up to the leading-edge and its angle is defined clockwise. The Latin Hypercube Sampling method (LHS) with an affine mapping is used to generate initial sampling points $N_{samples}$ in this (θ, x_{slot}) design space. The initial number of sampling points are supposed to be 40 points. Then, the CFD realizations (Section 4) are performed for the given sampling points to calculate the lift coefficient and the total length of the cavity appeared on the hydrofoil. Therefore, the lift coefficient and the total length of the cavity are our two objective functions. The lift coefficient function is represented by $C_l = f(x_{slot}, \theta)$ and the total length of cavity is denoted by $L_c = g(x_{slot}, \theta)$ will be found using a deep ANN (Section 3) which is exploited to construct the surrogate model. The lift coefficient can be calculated using the integral of the pressure in the direction perpendicular to the far-field flow divided by $0.5\rho u_\infty^2$. In the case of the total length of the cavity L_c , it will be calculated using the following relation:

$$L_c = L_{c_1} + L_{c_2} \quad (1)$$

where L_{c_1} denotes the length of the leading-edge cavity and L_{c_2} is the length of the mid-chord cavity. The leading-edge cavity is a cavity formed on the front hydrofoil, and the mid-chord cavity is a cavity that appeared on the rear hydrofoil created by slotting the original hydrofoil. The length of the leading-edge/mid-chord cavity is the horizontal distance between two points where the

pressure over the hydrofoil becomes lower than the vapor pressure and where it becomes higher than the vapor pressure.

The two objective functions of $C_l = f(x_{slot}, \theta)$ and $L_c = g(x_{slot}, \theta)$ will serve as an input to a genetic algorithm (GA) to result in an accurate and fast optimization scheme. The Pareto front comes out from GA with N_{parto} design points. These procedures are repeated N_{GA} times. In each iteration, the N_{parto} new design points will be added to the sample points, i.e., $N_{samples}$ will be updated to $N_{samples} + N_{parto}$. Subsequently, CFD realizations, deep ANN, and GA will be carried out. Here, $N_{GA} = 5$ is set which means that five generations are considered in the genetic algorithm. The number of new design points will not be greater than $N_{parto,max} = 20$ in each iteration, and if not, 20 points will be selected randomly. The latter is presumed to reduce the computational cost. This optimization procedure/algorithm is illustrated in Fig. 2.

This optimization procedure is performed in Matlab. The information of the sampling points will be automatically transformed into a meshing tool which is Gambit to generate the mesh for the CFD tool. The CFD tool is also a homemade code using the Frick method and C++ as a programming language (Section 4).

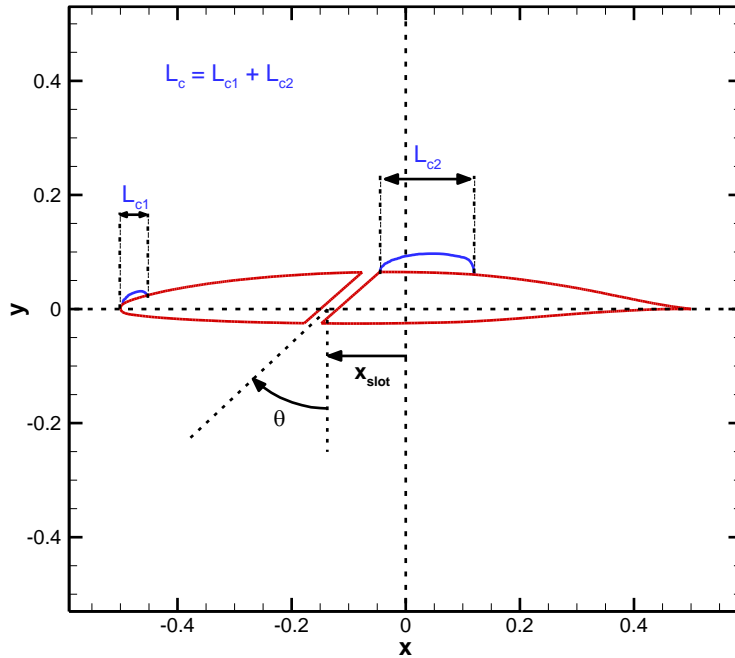


Fig. 1 Nomenclatures related to the optimization parameters, the total length of the cavity, the length of the leading-edge cavity, and the length of the mid-chord cavity.

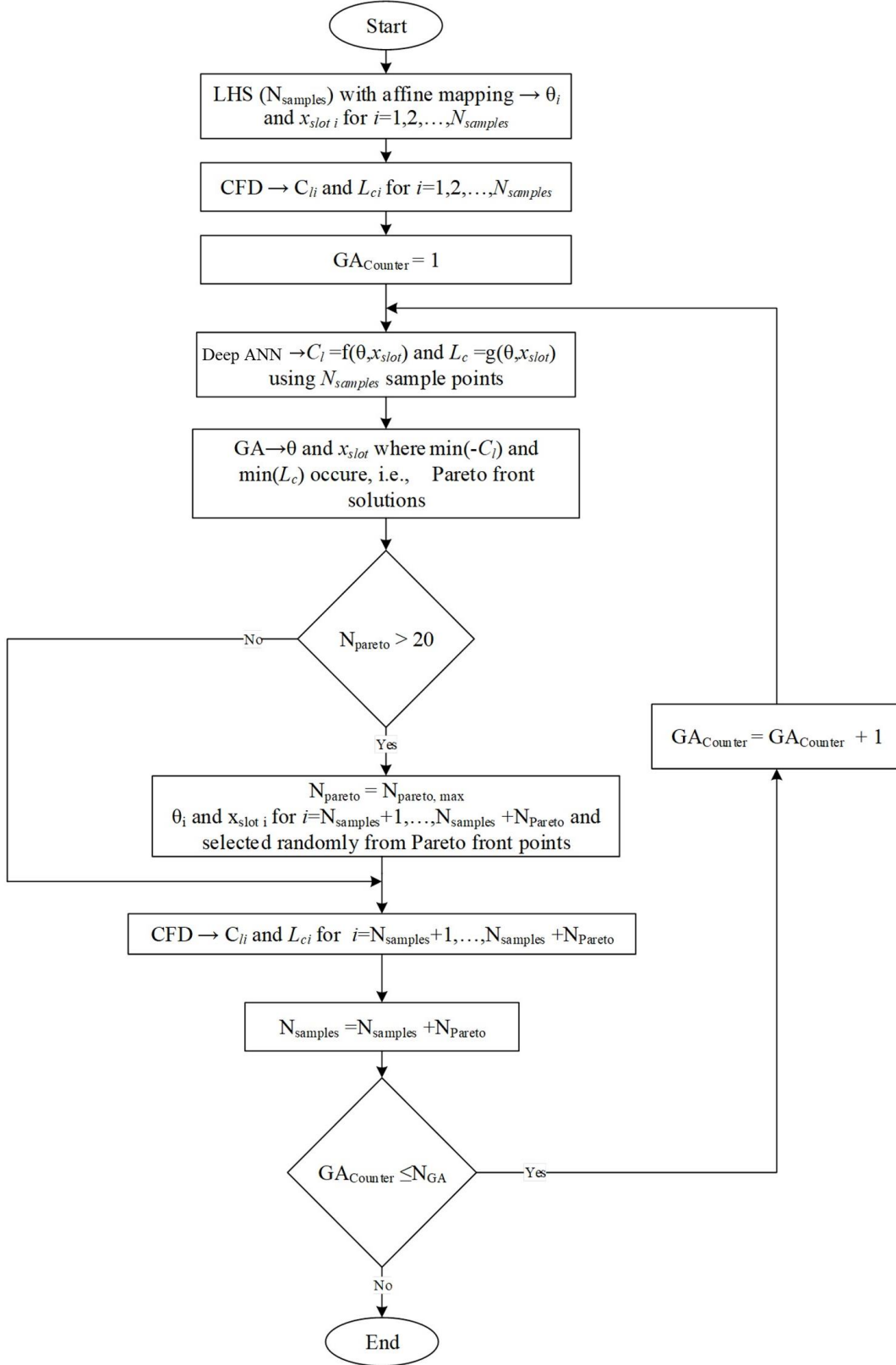


Fig. 2 Optimizer flowchart.

3. Surrogate model (deep ANN)

Knowing N_{LHS} input values for θ and x_{slot} using LHS method and their association target output values of $C_l = f(x_{slot}, \theta)$ and $L_c = g(x_{slot}, \theta)$ using the CFD tool, a deep ANN can be trained. The training dataset is created by 80% of data while the remaining 20% of data is used to verify the trained network. The preprocessing on the training dataset should be done before training a deep ANN. This preprocessing includes the normalization of data to the interval of [0,1]. Normalization increases the accuracy and speed of the ANN.

The first layer of the designed ANN is an input layer with two features (θ and x_{slot}). This layer is connected to a triple-layer that will be repeated N_r times. The first layer in this triple layer is a fully connected layer with N_n neurons. The next one is the leaky Rectified Linear Unit (ReLU) that can be efficiently employed for the regression jobs. The last one in the triple-layer is the batch normalization layer aiming to reduce errors of the ANN and increase its accuracy by retaining numbers throughout the ANN on the same scale. After repeating this triple-layer N_r times, then a fully connected layer is used to give out the data to the last layer which is the regression layer to estimate $C_l = f(x_{slot}, \theta)$ and $L_c = g(x_{slot}, \theta)$. A schematic of the designed deep ANN is shown in Fig. 3.

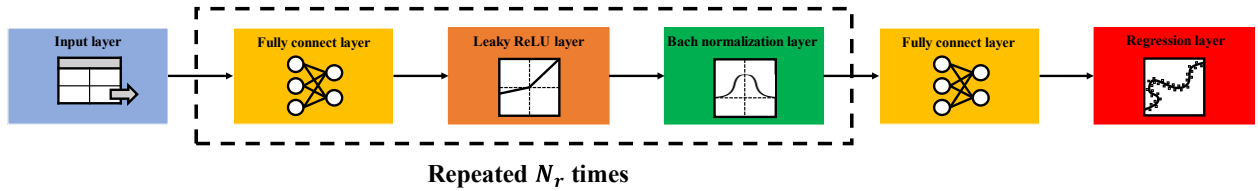


Fig. 3 Architecture of the designed ANN network

A residual minimizer is performed to properly adjust the weights and biases of the deep ANN. The residual minimizer tries to minimize a loss function indicating the differences between the deep ANN outputs (estimated surrogate models at the sample points) and the target outputs (CFD results). The Adam method is selected as the residual minimizer. The number of epochs in the Adam method is 250 and the learning rate equals 0.08. Our study shows that these values for epochs and learning rate leads to an accurate and fast deep ANN.

The number of repeated triple-layers is $N_r = 4$ and the number of neurons is $N_n = 30$, which plus prescribed deep ANN settings leads to not getting stuck on overfitting and underfitting problems.

4. Simulator

Steady inviscid cavitating fluid flows can be mathematically described using preconditioned Euler equations with the artificial compressibility method as follows:

$$\mathbf{\Pi} \frac{\partial \mathbf{Q}}{\partial \tau} + \frac{\partial \mathbf{F}}{\partial x} + \frac{\partial \mathbf{G}}{\partial y} - \mathbf{S}_c = 0 \quad (2)$$

where $\mathbf{\Pi}$ indicates the preconditioning matrix which is

$$\mathbf{\Pi} = \begin{bmatrix} \frac{1}{\rho_m \beta^2} & 0 & 0 & 0 \\ 0 & \rho_m & 0 & u \Delta \rho_l \\ 0 & 0 & \rho_m & v \Delta \rho_l \\ \frac{\alpha_l}{\rho_m \beta^2} & 0 & 0 & 1 \end{bmatrix} \quad (3)$$

The artificial time is denoted by τ and derivatives with respect to this variable should go to zero for satisfying the consistency and convergence conditions. This means that this formulation can be used only for steady-state solutions. This is corresponding with the physics we are dealing with because we are going to optimize a hydrofoil experiencing quasi-steady sheet cavitation flow. The cavitation source term \mathbf{S}_c plays an important rule in cavitation modeling and it is defined in a way to appropriately model the mass transfer between the liquid and vapor phases that occurred in the cavitation process. We will further discuss this term in the next section. The flux vectors $\mathbf{H} = (\mathbf{F}, \mathbf{G})$ and the solution vector \mathbf{Q} are written as follows:

$$\mathbf{Q} = \begin{bmatrix} p \\ u \\ v \\ \alpha_l \end{bmatrix}, \quad \mathbf{F} = \begin{bmatrix} u \\ \rho_m u^2 + p \\ \rho_m uv \\ \alpha_l u \end{bmatrix}, \quad \mathbf{G} = \begin{bmatrix} v \\ \rho_m uv \\ \rho_m v^2 + p \\ \alpha_l v \end{bmatrix} \quad (4)$$

The solution vector is consisting of the pressure p , the velocity vector (u, v) , and the liquid volume fraction α_l . The subscribes l, v , and m are added to facilitate identifying the liquid, vapor, and mixture states. While the liquid density ρ_l and ρ_v are supposed to be constant, the mixture density is allowed to vary according to the relation $\rho_m = \alpha_l \rho_l + \alpha_v \rho_v$. Note that the summation of volume fraction of different phases is always unity, i.e., $\alpha_l + \alpha_v = 1$. Moreover, $\rho_l = 1$ and $\rho_v = 0.01$ are used here that prove to be suitable values for simulating cavitating flows in a water medium. In Eq. (3), the density jump is indicated by $\Delta \rho_l = \rho_l - \rho_v$.

Following the concept of the artificial compressibility method, the coefficient denoted by β is used in the governing equations to tackle the pressure-velocity coupling problem pertaining to incompressible flows. It is a user-defined parameter and here we simply use a constant value $\beta = 3$ similar to [36], [41].

4.1. Cavitation modeling

As mentioned in the previous section, the cavitation process is modeled by the cavitation source term S_c which is

$$S_c = \begin{bmatrix} (\dot{m}^+ + \dot{m}^-) \left(1 - \frac{1}{\rho_v}\right) \\ 0 \\ 0 \\ \dot{m}^+ + \dot{m}^- \end{bmatrix} \quad (5)$$

where \dot{m}^- models the evaporation phenomena which is the mass transfer from the liquid to the vapor phase, and it is vice versa for \dot{m}^+ which represents the condensation process wherein the vapor phase transits to the liquid phase. These two variables are differently defined in the literature [42]–[46]. Here, the relations proposed by Merkel et al. [42] is exploited, i.e.,

$$\begin{aligned} \dot{m}^+ &= \left(\frac{C_{prod}}{t_\infty}\right) (1 - \alpha_l) \text{Max}(0, p - p_v) \\ \dot{m}^- &= \left(\frac{C_{dest}}{t_\infty}\right) \frac{1}{\rho_v} \alpha_l \text{Min}(0, p - p_v) \end{aligned} \quad (6)$$

These relations have been proposed by Merkel et al. [42] that derived from their experimental work. Numerical studies [36], [47] show that these relations are reliable and accurate for simulating cavitating flows. The parameters C_{prod}/t_∞ and C_{dest}/t_∞ are the constant parameters which control the liquid production and destruction rates, respectively. They are user-defined parameters where $C_{prod}/t_\infty = 1$ and $C_{dest}/t_\infty = 80$ are used here. Numerical studies done in literature [36], [47] prove these values lead to accurate numerical results. Finally, the vapor pressure p_v is obtained according to the predefined cavitation number $\sigma = 2(p_\infty - p_v)$ where p_∞ is the pressure far enough from the hydrofoil surface which is assumed unit. Note that all the variables used in the present study are non-dimensional identical to the ones presented in [36].

4.2. Spatial discretization

So that being able to simulate cavitating flows, we should suitably address the solution of the governing equation (2) by means of a numerical method. Here, the Frink numerical method is used to discretize the spatial derivative terms in the governing equations.

By integrating Eq. (2) through the surface A of an element, it can be rewritten as

$$\int_A \left[\Pi \frac{\partial Q}{\partial \tau} + \frac{\partial(F)}{\partial x} + \frac{\partial(G)}{\partial y} - S_c \right] dA = 0 \quad (7)$$

In the finite volume method variables are assumed to be constant through an element, then

$$\int_A \Pi \frac{\partial Q}{\partial \tau} dA = \Pi \frac{\partial Q}{\partial \tau} A \quad (8)$$

For the spatial derivative of inviscid fluxes, we have

$$\int_A \left[\frac{\partial F}{\partial x} + \frac{\partial G}{\partial y} \right] dA = \int_A [\nabla \cdot \mathbf{H}] dA \quad (9)$$

and then using the divergence theorem applied to triangular domain results in

$$\int_A [\nabla \cdot \mathbf{H}] dA = \oint_{\partial A} [\mathbf{H}^* \cdot \hat{\mathbf{n}}] dL = \sum_{k=1}^{N_{faces}=3} (\mathbf{H}^* \cdot \hat{\mathbf{n}})_k L_k \quad (10)$$

where \mathbf{H}_k^* is the numerical flux for the k -th face of the element, and it depends on the flux vectors in two neighboring elements sharing that face. After finding the flux vectors in two neighboring elements by exploiting the Frink numerical method, the Lax numerical flux method is used to calculate the numerical flux. The calculation of the Lax numerical flux method will be explained later. Variable $\hat{\mathbf{n}}$ is the normal outward vector. The face length of the triangle element is denoted by L .

The integration of the cavitation source term S_c can be written as

$$\int_A S_c dA = S_c A \quad (11)$$

The integration of the artificial dissipation terms should be carefully evaluated, and it will be addressed in the next section. Finally, the discretization process, by substituting Eqs. (8)-(11) into (7), results in

$$\frac{\partial \mathbf{Q}}{\partial \tau} = \frac{\mathbf{\Pi}^{-1}}{A} \left[\mathbf{S}_c A - \sum_{k=1}^{N_{faces}} (\mathbf{H}^* \cdot \hat{\mathbf{n}})_k L_k \right] = \mathbf{R} \quad (12)$$

where R is called the right-hand side vector.

4.2.1. The Frink numerical method

The higher-order finite volume methods can be derived using reconstructing fluxes at the element faces. To show how the Frink numerical method can be used to increase the order of accuracy of the solution from the first-order in the classical finite volume method to the second-order one, refer to Fig. 4. While in the classical first-order finite volume methods variables at the faces can be read as $q_{f_1} = q_{f_2} = q_{f_3} = q_c$, in the Frink numerical method [39], they are reconstructed as follows:

$$\begin{aligned} q_{f_1} &= q_c + \frac{1}{3} \left[\frac{1}{2} (q_{n_1} + q_{n_2}) - q_{n_3} \right] \\ q_{f_2} &= q_c + \frac{1}{3} \left[\frac{1}{2} (q_{n_2} + q_{n_3}) - q_{n_1} \right] \\ q_{f_3} &= q_c + \frac{1}{3} \left[\frac{1}{2} (q_{n_1} + q_{n_3}) - q_{n_2} \right] \end{aligned} \quad (13)$$

The remaining variables to be defined are the nodal values denoted by q_{n_1} , q_{n_2} , and q_{n_3} . An area-weighted average, among the elements sharing the node, is used to calculate values in nodes.

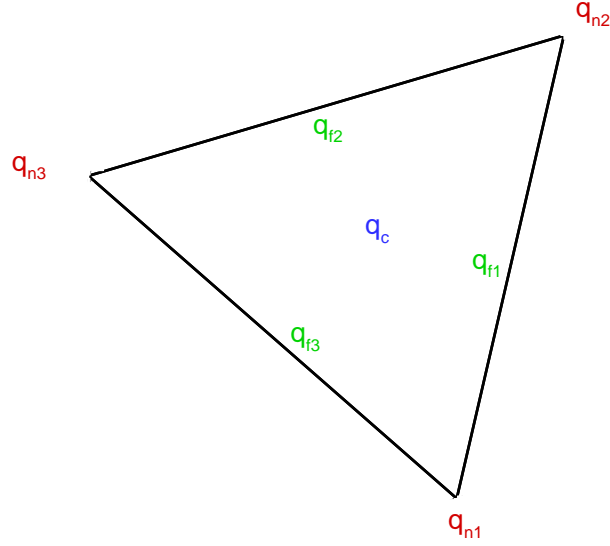


Fig. 4 Nomenclatures used for constructing fluxes in the Frink numerical method.

4.2.2. Numerical flux

The Lax numerical flux is used here to address the Riemann problem for the jumps between two neighboring elements. If the flux in a face is denoted by the subscript L and its neighbor's value by R , then

$$\mathbf{H}_k^* = \frac{1}{2}(\mathbf{H}_L + \mathbf{H}_R - C\lambda\Pi(\mathbf{Q}_R - \mathbf{Q}_L)) \quad (14)$$

where λ is the largest eigenvalue of the system of equations

$$\lambda = \sqrt{u_L^2 + v_L^2} + \sqrt{u_L^2 + v_L^2 + \beta^2} \quad (15)$$

and C is a constant parameter with $C \leq 1$ for satisfying stability conditions. Selecting higher values for C means adding more dissipation to the solution domain that may cause reducing global accuracy. Here, $C = 0.25$ is used to consequently provides accuracy and stability needs.

4.2.3. Artificial dissipation

Although discretization has been done, we should care about the artificial non-physical oscillations that occur near the cavity zone which could make the solution unstable. To prevent such undesirable oscillations in the solution, the artificial dissipation term \mathbf{D} [40] is added to the right-hand side of Eq. (12) as follows:

$$\frac{\partial \mathbf{Q}}{\partial \tau} = \mathbf{R} + \mathbf{D} = \mathbf{R}' \quad (16)$$

The artificial dissipation for the j -th element can be written as:

$$\mathbf{D}_j = \sum_{k=1}^{N_{faces}=3} \mathbf{d}_{j_k} \quad (17)$$

where k indicates the face number. If the solution vector in neighbor element through the k -th face is shown by \mathbf{Q}_j^k , then the dissipation term can be written as follows:

$$\mathbf{d}_{j_k} = - \left(\frac{A_j}{\Delta \tau} + \frac{A_j^k}{\Delta \tau} \right) \left[\frac{\varepsilon_{j_k}}{2} (\mathbf{Q}_j - \mathbf{Q}_j^k) \right] \quad (18)$$

where $\Delta \tau$ is the artificial time step. The artificial viscosity coefficient ε has to be determined such that tends to zero where the solution is smooth and to a definite value in non-smooth regions which normally occur near the cavity zone which is the origin of the artifact oscillations generated due to the sharp jump in the density variable across the interface of the two phases. In order to determine the artificial viscosity coefficient, we follow the idea presented in Jameson et al. work [40] which is:

$$\begin{aligned} \varepsilon_{j_k} &= \kappa_\rho \gamma_{j_k} \\ \gamma_{j_k} &= \left| \frac{\rho_j - \rho_j^k}{\rho_j + \rho_j^k} \right| \end{aligned} \quad (19)$$

and $\kappa_\rho = 0.025$ is chosen here.

4.3. Temporal discretization

The Euler method is used here for discretizing the temporal derivative in Eq. (16)

$$\frac{Q^{m+1} - Q^m}{\Delta\tau} = R^m \quad (20)$$

where superscript m indicates the time-level.

5. Results

In this section, the numerical results are presented. The simulator is first evaluated in subsection 5.1 wherein the sheet/leading-edge and mid-chord cavitations have been simulated and are compared with the experimental data. After proving that the numerical method works fine, then the results for the slotted hydrofoil and its optimized shape will be discussed.

5.1. Validation

Once the original hydrofoil NACA 66(MOD) is slotted, instead of one cavity pocket over the original hydrofoil surface, two-cavity pockets might form over the modified hydrofoil. The first cavity pocket over the modified hydrofoil can be seen as a sheet/leading-edge cavity, and the second one is like the mid-chord cavity over the original hydrofoil. Thus, the sheet and mid-chord cavitation phenomenon are simulated here to show that the numerical method arranged here can be effectively used for the optimization of the slotted hydrofoil. The sheet cavitation will be created over the original hydrofoil when water flows over NACA 66 (MOD) at the angle of attack $\alpha = 4^\circ$ and cavitation number $\sigma = 0.84$, and by considering $\alpha = 1^\circ$ and $\sigma = 0.43$ the mid-chord cavitation will be formed.

In Fig. 5, the generated grid with 16330 triangle elements is shown. The grid type is chosen to be triangular because they can be used over arbitrary and complex geometries such as the cases we are dealing with in this paper, i.e., slotted hydrofoil. Moreover, they are suitably working in inviscid flows, because there is no need for having high-resolution grids close to the walls due to the absence of the boundary layer. As can be seen in Fig. 5, the radius of the far-field boundary is assumed ten times of the hydrofoil chord. Moreover, a finer grid is used close to the hydrofoil surface while a coarser grid is used far from its surface. Using high-resolution grids near the hydrofoil will help to sharply capture the cavity pocket, and a coarse grid near the far-field boundary will aid to damp the artificial incoming and outgoing waves occurred there.

In Fig. 6, the numerical results for the simulation of the sheet cavitation over the original NACA 66 (MOD) hydrofoil are illustrated. The density, pressure, and velocity magnitude contours indicate that the cavitation phenomenon can be expected over the suction side of the hydrofoil wherein the velocity magnitude is increased and subsequently the pressure is decreased to a lower value than the vapor pressure. Moreover, the velocity magnitude immediately reduces when the cavity pocket is closed which is a sign for the re-entrant jet. In Fig. 7, the calculated surface pressure coefficient by the present numerical method is compared with the experimental data [48]. As can be seen in this figure, the agreement between numerical results is satisfactory. The pressure in the cavity pocket remains unchangeable that excellently follows experimental pieces of evidence. In addition, the pressure recovery at the trailing edge is captured by the present numerical method efficiently.

In Fig. 8 the density, pressure and velocity magnitude contours for the mid-chord cavitation type has been plotted. As shown the cavitation does not start from the leading-edge, but starts from the middle of the suction side. In Fig. 9, the numerical results by utilizing the Frink numerical method are shown and compared with the experimental data [48] for this cavitation type. As shown in this figure, the numerical results obey the expected physical behaviors and also agree with the experimental data.

From the obtained numerical results for the simulation of these two cavitation types, it can be concluded that the numerical framework set up here can be used to effectively simulate different quasi-steady cavitation flows encountered in the present study.

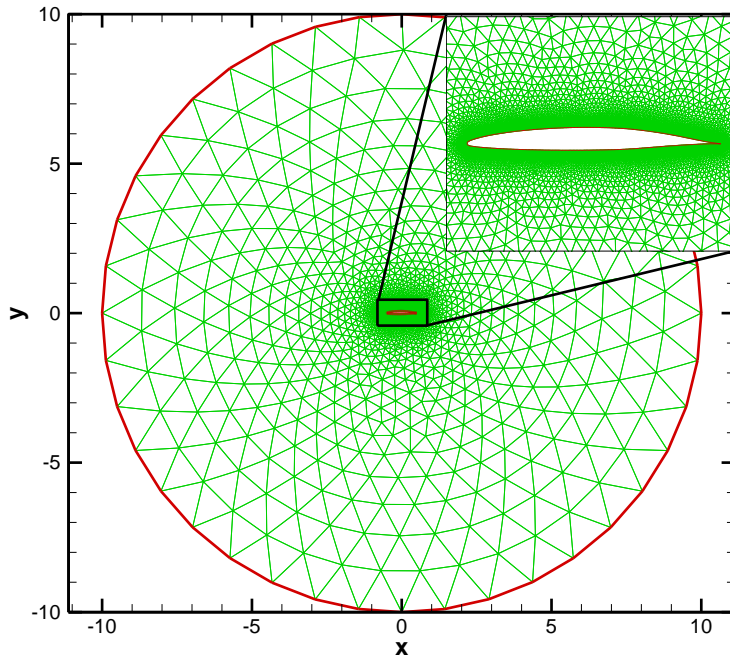
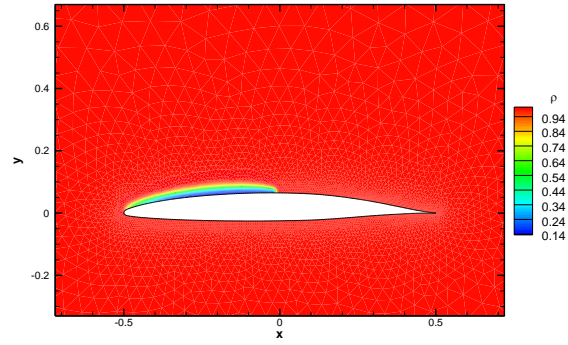
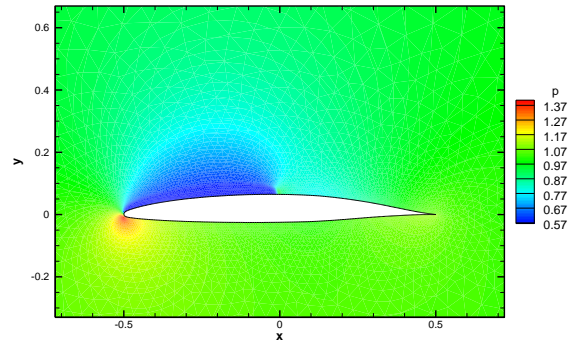


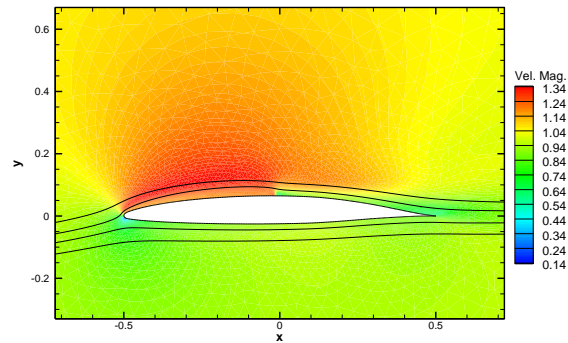
Fig. 5 Generated grid for the original NACA 66 (MOD) hydrofoil.



(a)



(b)



(c)

Fig. 6 Contours of a) the density, b) the pressure, and c) the velocity magnitude with the streamlines computed by the Frink numerical method for the problem of cavitating flow over NACA 66 (MOD) at $\sigma = 0.84$ and $\alpha = 4^\circ$.

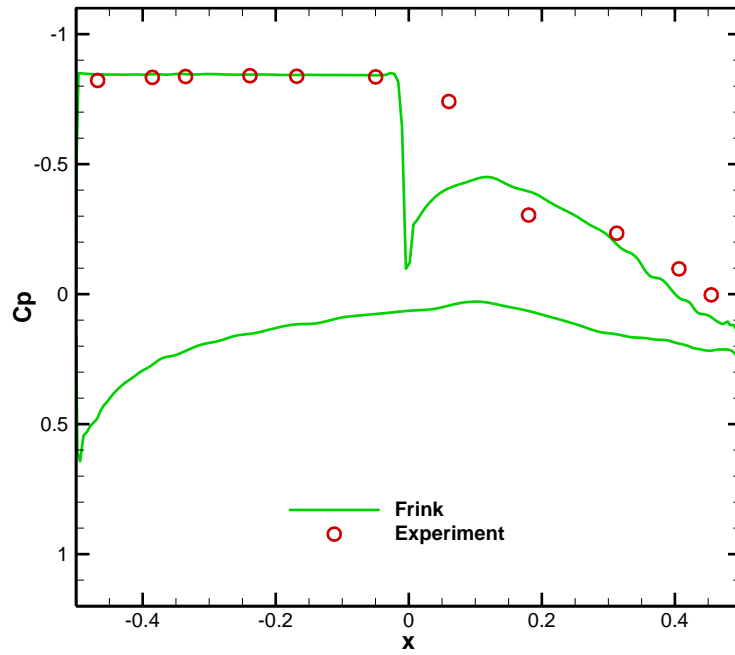
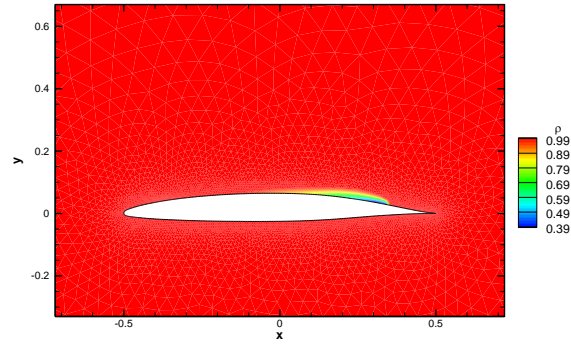
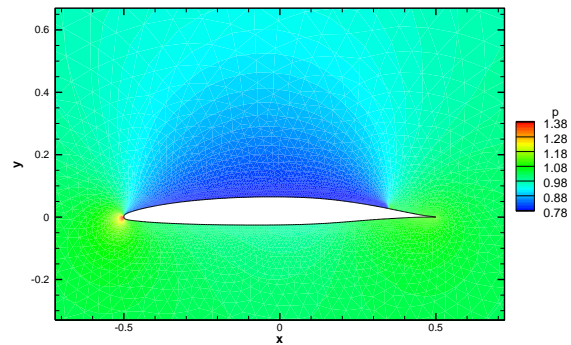


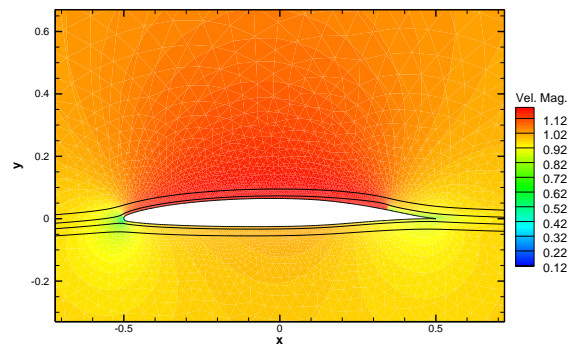
Fig. 7 Comparison of the pressure coefficient obtained by the Frink numerical method and experimental data [48] for the problem of cavitating flow over NACA 66 (MOD) at $\sigma = 0.84$ and $\alpha = 4^\circ$.



(a)



(b)



(c)

Fig. 8 Contours of a) the density, b) the pressure, and c) the velocity magnitude with the streamlines computed by the Frink numerical method for the problem of cavitating flow over NACA 66 (MOD) at $\sigma = 0.43$ and $\alpha = 1^\circ$.

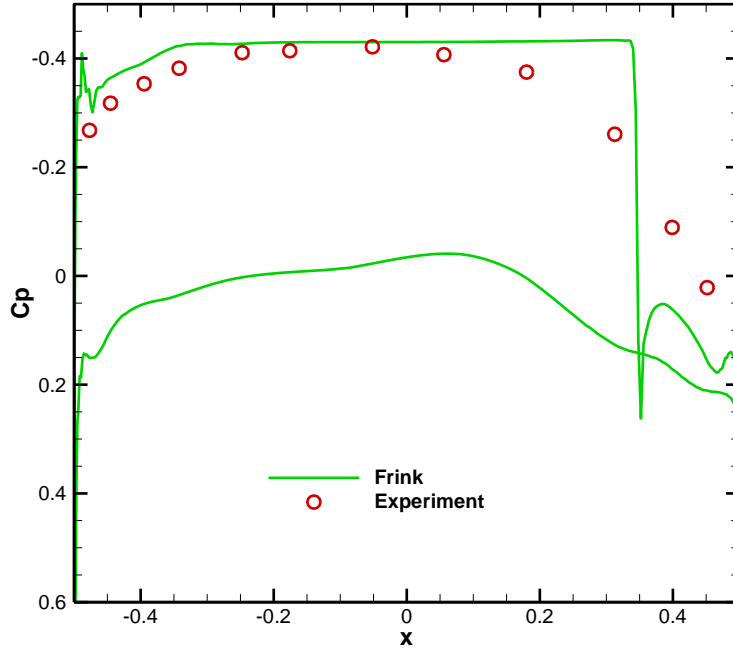


Fig. 9 Comparison of the pressure coefficient obtained by the Frink numerical method and experimental data [48] for the problem of cavitating flow over NACA 66 (MOD) at $\sigma = 0.43$ and $\alpha = 1^\circ$.

5.2. Optimization of slotted hydrofoil

The goal of this study is to optimize the slotted NACA 66 (MOD) hydrofoil immersed in water at cavitation number $\sigma = 0.84$ and angle of attack $\alpha = 4^\circ$. As discussed in detail in the optimization procedure, 40 initial sampling points are used to start the optimization process. These initial sampling points are obtained by employing the LHS method, and these points are depicted in Fig. 10(a). By advancing in the optimization process, new design points will be added to the initial sampling points to create and assess the objective functions and to finally find out the optimum points. All the points used in the optimization process are illustrated in Fig. 10(b) and it can be seen that many new points are inserted in the upper right side of the figure where the slots are created close to the leading-edge with higher angles. It means that the optimizer seeks the optimal point there, and by adding many new points in that region, it improves the high-fidelity model.

In Fig. 11, the contours related to L_{c_1} and L_{c_2} obtained using the deep ANN are shown. From Fig. 11(a) it can be concluded that generally at a given slot location the leading-edge cavity

will reach its minimum size around $\theta = 45^\circ$, while lower and higher angles than this angle will cause having larger leading-edge cavity size. At a given slot angle, moving the slot location from the middle to the leading-edge will favorably result in decreasing in L_{c_1} . Thus, smaller L_{c_1} will be found around $\theta = 45^\circ$ and high slot angles.

In the case of L_{c_2} , as depicted in Fig. 11(b), at a given slot location the mid-chord cavity will reach its maximum size around $\theta = 60^\circ$, while lower and higher angles than this angle will cause having larger leading-edge cavity size. At a given slot angle, by increasing the slot location, L_{c_2} will disadvantageously increase. Thus, for having smaller L_{c_2} , higher slot angles should be used with a slot placed around the middle of the hydrofoil.

The contours of the objective functions C_l and L_c are illustrated in Fig. 12. The objective functions are purely non-linear with respect to optimization parameters. This figure can be very useful for engineers when they are designing artifacts to find out a design point passing their presumed criteria and to figure out how changing the design point would affect the performance of the artifact.

According to the results plotted in Fig. 12, we can roughly argue that there are two domains where L_c becomes minimum

$$\begin{aligned} Dom(L_{c_{min}})_1 &= \{(\theta, x_{slot}) \in \mathbb{R} | 25^\circ < \theta < 65^\circ, 0 < x_{slot} < 0.15\} \\ Dom(L_{c_{min}})_2 &= \{(\theta, x_{slot}) \in \mathbb{R} | 72.5^\circ < \theta < 85^\circ, 0.1 < x_{slot} < 0.4\} \end{aligned} \quad (21)$$

and there is one domain that C_l becomes maximum

$$Dom(C_{l_{max}}) = \{(\theta, x_{slot}) \in \mathbb{R} | 40^\circ < \theta < 85^\circ, 0.15 < x_{slot} < 0.4\} \quad (22)$$

Then, it is expected that the optimized points placed in the set stated hereunder:

$$\begin{aligned} &(Dom(C_{l_{max}}) \cap Dom(L_{c_{min}})_1) \cup (Dom(C_{l_{max}}) \cap Dom(L_{c_{min}})_2) \\ &= \{(\theta, x_{slot}) \in \mathbb{R} | 72.5^\circ < \theta < 85^\circ, 0.15 < x_{slot} < 0.4\} \end{aligned} \quad (23)$$

which is exactly corresponding with the domain that the optimizer seeks for the optimal points as depicted in the right upper part of Fig. 10(b). It is evident that the optimization process is suitably designed and works appropriately. Before presenting the optimal points, it is important to assess the accuracy of the surrogate model and its validity. For this aim, at different points than the trained dataset, along the midlines of the design space, the CFD results are compared with the data

extracted from the surrogate model that are given in Table 1. The percentage of the error is defined as

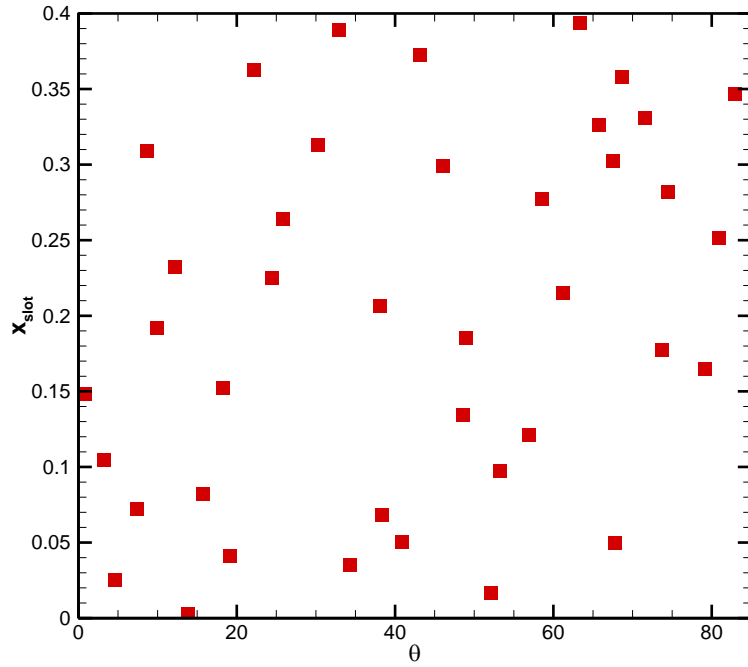
$$\begin{aligned}
 Error(L_c) &= \frac{|L_{cCFD} - L_{c\text{surrogate}}|}{L_{cCFD}} \times 100 \\
 Error(C_l) &= \frac{|C_{lCFD} - C_{l\text{surrogate}}|}{|C_{lCFD}|} \times 100
 \end{aligned} \tag{24}$$

and it is seen that the maximum percentage of the error in predicting L_c is lower than 4.06 percent, while for C_l this error is lower than 2.24. These amounts of errors are in an acceptable range, and it can be concluded that the surrogate model is trained properly and is reliable. In Figs. 13 and 14, the density and pressure contours for points used in Table 1 are plotted. From Fig. 13 and Table 1 it can be deduced that for $\theta = 42.5^\circ$ and by pushing the slot from the middle chord to the leading-edge, the lift coefficient is desirably increased while the total length of cavity is unfavorably increased. However, from Fig. 14 and Table 1 it can be seen that for $x_{slot} = 0.2$ and by increasing the slot angle, while L_c is always desirably decreasing, C_l is first decreasing and then increasing.

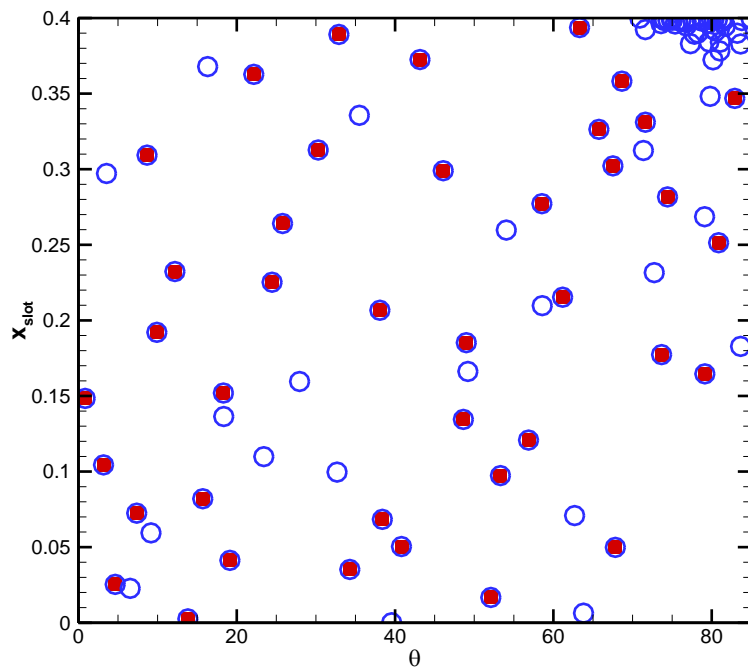
In Table 2, the output of the optimization process, which is the final Pareto front, is given. While any point in the Pareto front is a candidate to be served as an optimal point, another criterion should be added to help the optimal point selection. This criterion is arbitrary. Here, we are seeking a point that shows the best performance in comparison with the average values of all points in the Pareto front. These average values are indicated by \bar{L}_c and \bar{C}_l and are presented in the last row. In other words, the optimal point would be a point with $\max(\bar{L}_c - L_c)$ and $\max(C_l - \bar{C}_l)$ which is achieved for $(\theta, x_{slot}) = (80.461, 0.354)$.

In Fig. 15, generated grid for this optimal slotted hydrofoil is shown where, similar to the original hydrofoil illustrated in Fig. 5, a finer grid resolution is utilized close to the hydrofoil surface in comparison with the ones far enough from it. The pressure contour with streamlines and the density contour is shown in Fig. 16. It can be seen that by the slot the fluid with higher-pressure on the lower surface of the hydrofoil is transferred to the suction side with lower pressure resulting in shrinking the cavity pocket. In fact, the high-pressure fluid is injected to the suction side with lower-pressure and prevents the pressure becoming lower than the vapor pressure and subsequently results in not to happen cavitation. However, injecting a high-pressure fluid over the

hydrofoil will decrease the lift coefficient. This phenomenon can be clearly seen in Fig. 17 where the pressure coefficient over the surface of the optimized slotted hydrofoil is compared with the original hydrofoil. In this way, we can favorably shrink the cavity pocket, but the lift coefficient will be disadvantageously decreased. Basically, imposing higher pressure over the upper surface of the hydrofoil will cause a downward force that means decreasing in the lift. The total length of the cavity that appeared on the suction side for the optimized slotted hydrofoil is $L_c = 0.2006$, while it is 0.482 for the original hydrofoil that shows an improvement. In the case of the lift coefficient, it equals 0.6098 for the optimized slotted hydrofoil while it is 0.688 for the original hydrofoil that shows a deterioration. These results indicate that with a penalty of about 11.4% in the lift coefficient, it is possible to decrease the cavity size by about 58.4%.

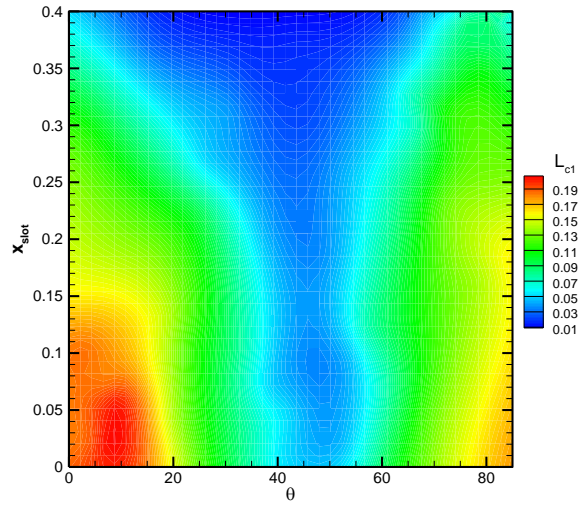


(a)

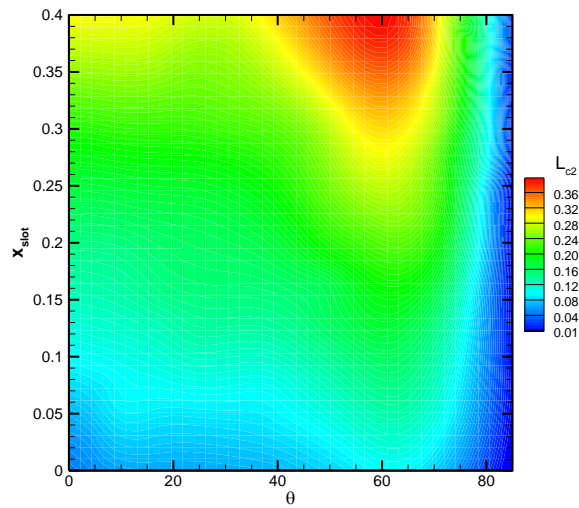


(b)

Fig. 10 a) Initial sampling using 40 points and b) final training samples.

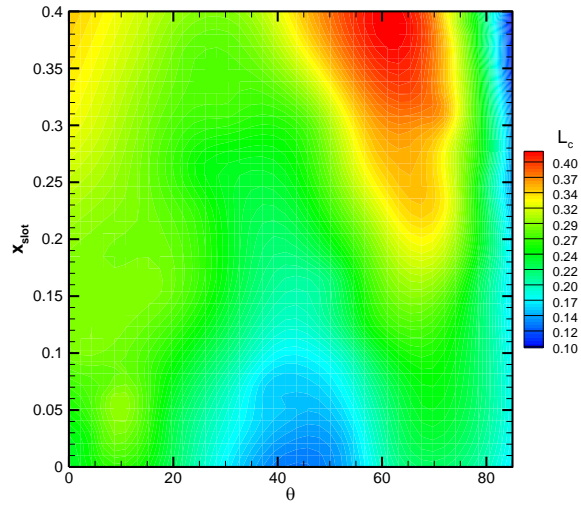


(a)

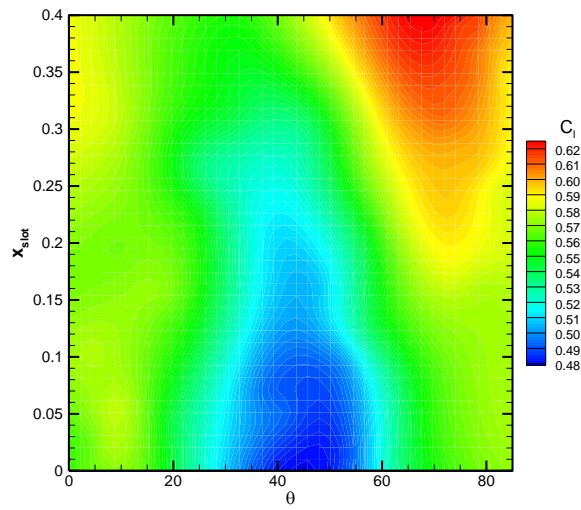


(b)

Fig. 11 Contours for a) L_{c1} and b) L_{c2} obtained using the fitting method.



(a)



(b)

Fig. 12 Contours for a) L_c and b) C_l obtained using the fitting method.

Table 1 Investigation of the accuracy of the surrogate model

θ	x_{slot}	CFD		Surrogate model		Error (%)	
		L_c	C_l	L_c	C_l	L_c	C_l
42.5°	0.00	0.118	0.476	0.123	0.484	4.778	1.591
42.5°	0.20	0.231	0.519	0.222	0.514	3.723	0.966
42.5°	0.40	0.323	0.564	0.339	0.577	4.978	2.244
0.0°	0.20	0.284	0.574	0.297	0.575	4.532	0.068
42.5°	0.20	0.231	0.519	0.222	0.514	3.723	0.966
85.0°	0.20	0.157	0.584	0.162	0.586	2.852	0.286

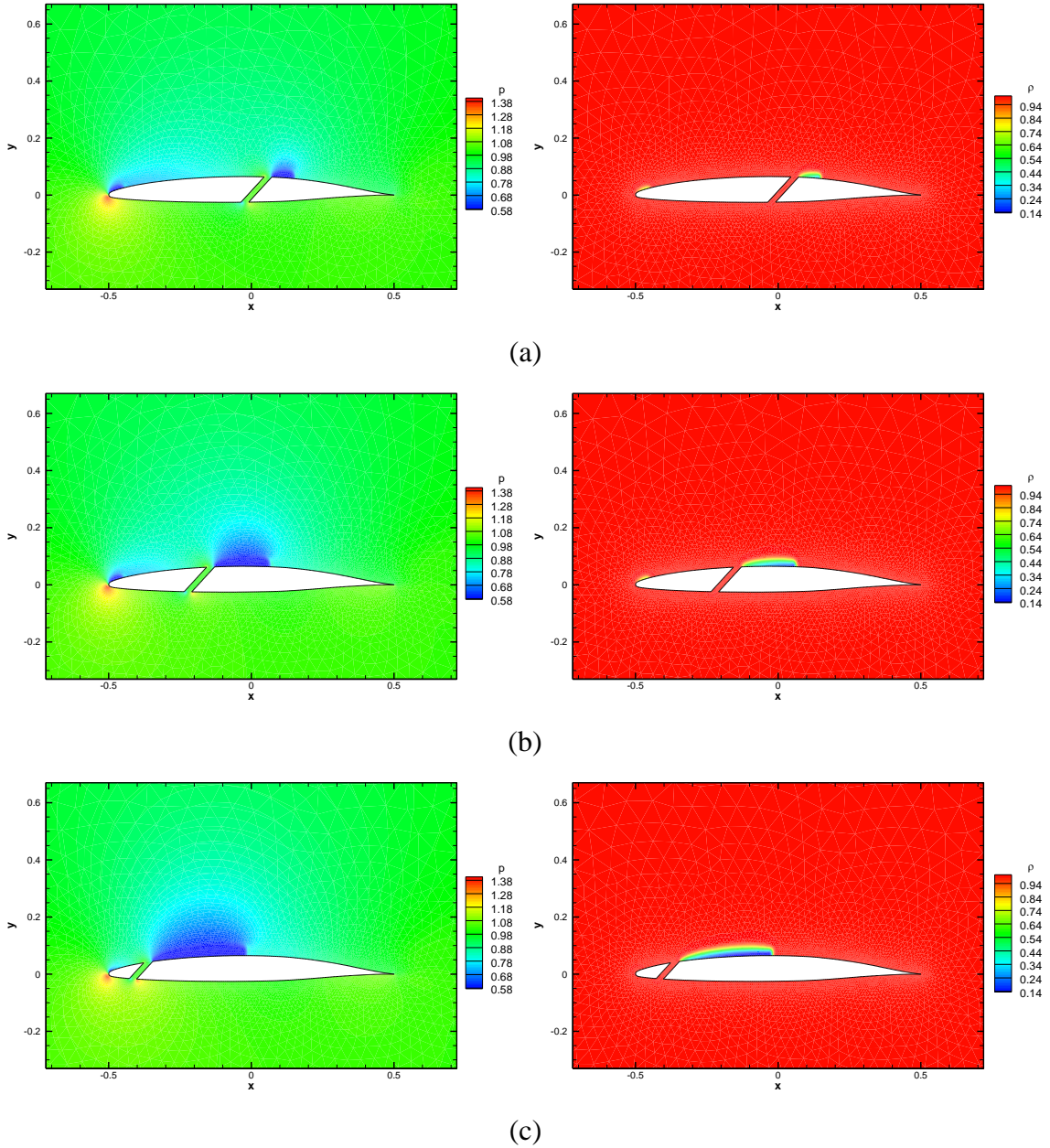
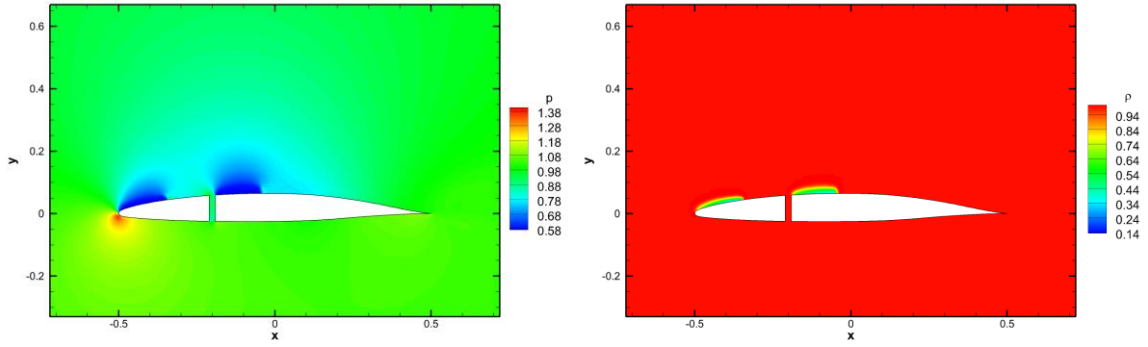
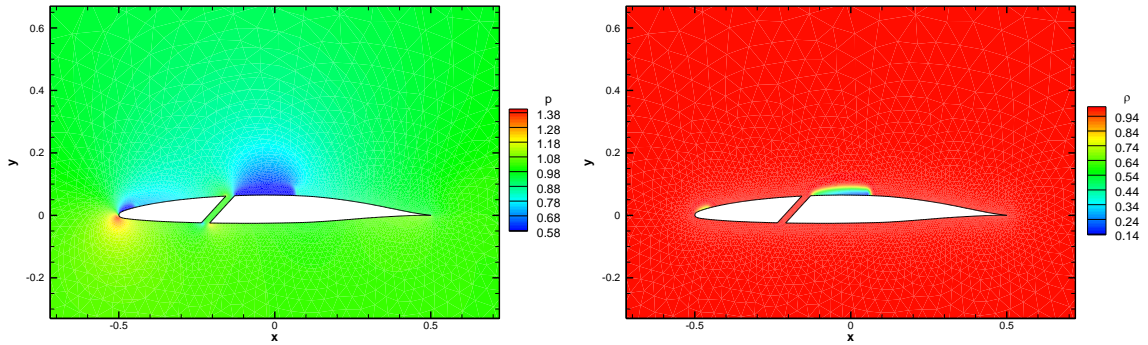


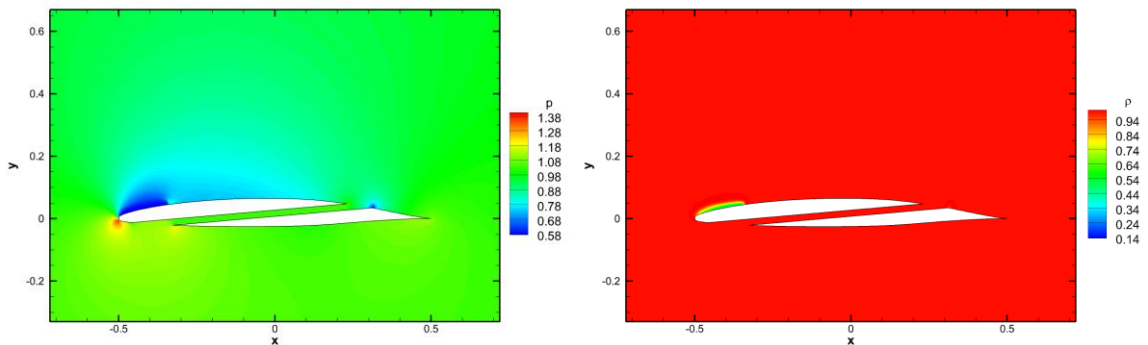
Fig. 13 The pressure (left column) and density (right column) contours for $\theta = 42.5^\circ$ and a) $x_{slot} = 0.0$, b) 0.2, and c) 0.4



(a)



(b)



(c)

Fig. 14 The pressure (left column) and density (right column) contours for $x_{slot} = 0.2$ and a) $\theta = 0.0^\circ$, b) 42.5° , and c) 85.0° .

Table 2 Pareto front design points (GA output)

θ	x_{slot}	L_c	C_l	$\bar{L}_c - L_c$	$C_l - \bar{C}_l$	
84.545	0.003	0.1293	0.5976	0.0814	-0.0119	
80.780	0.094	0.1945	0.6091	0.0162	-0.0005	
79.936	0.192	0.2107	0.6112	0.0001	0.0017	
78.943	0.138	0.2295	0.6132	-0.0187	0.0036	
75.576	0.146	0.2882	0.6169	-0.0775	0.0073	
80.461	0.354	0.2006	0.6098	0.0102	0.0003	Selected
79.473	0.284	0.2196	0.6123	-0.0089	0.0028	
76.866	0.339	0.2676	0.6164	-0.0569	0.0068	
82.397	0.111	0.1648	0.6046	0.0460	-0.0050	
78.373	0.198	0.2402	0.6143	-0.0295	0.0047	
77.263	0.247	0.2605	0.6158	-0.0497	0.0063	
82.786	0.003	0.1578	0.6033	0.0529	-0.0063	
82.999	0.047	0.1542	0.6027	0.0566	-0.0069	
83.464	0.202	0.1465	0.6014	0.0643	-0.0082	
78.811	0.302	0.2322	0.6136	-0.0215	0.0041	
76.170	0.073	0.2786	0.6165	-0.0679	0.0070	
84.996	0.001	0.1228	0.5961	0.0880	-0.0135	
75.117	0.400	0.2958	0.6173	-0.0850	0.0077	
		$\bar{L}_c = 0.2107$	$\bar{C}_l = 0.6096$			

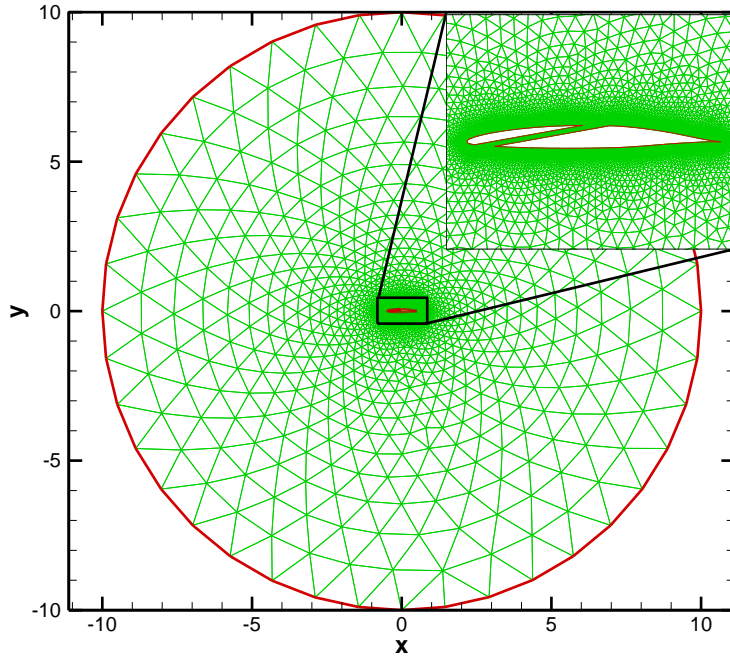
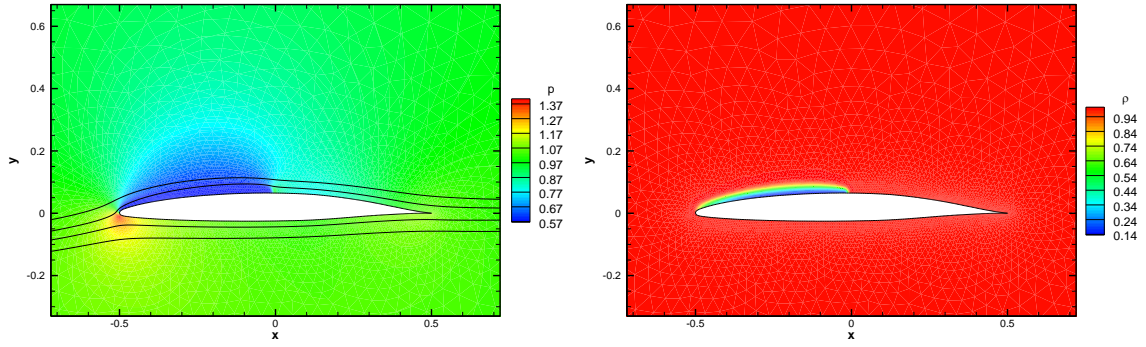
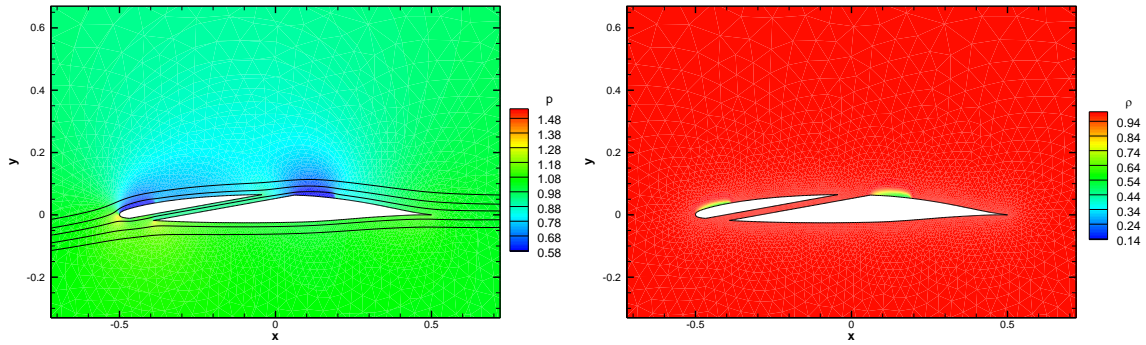


Fig. 15 Generated grid for the optimal slotted NACA 66 (MOD) hydrofoil.

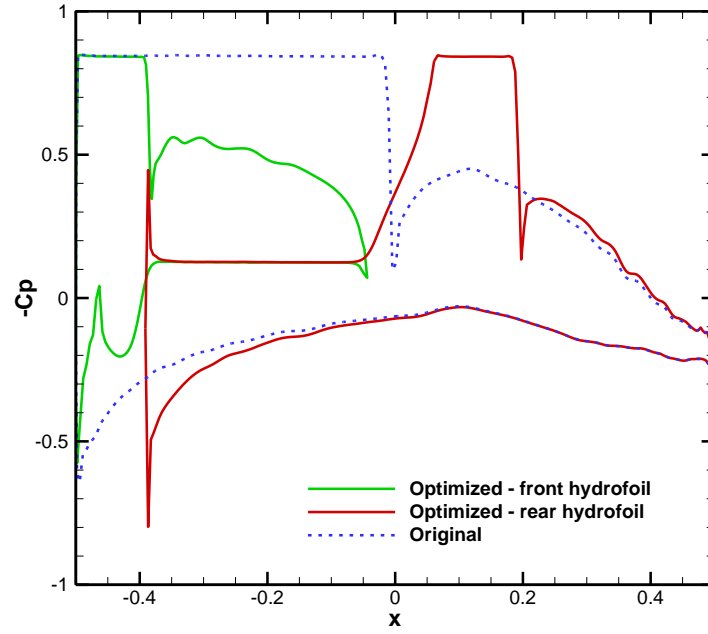


(a)

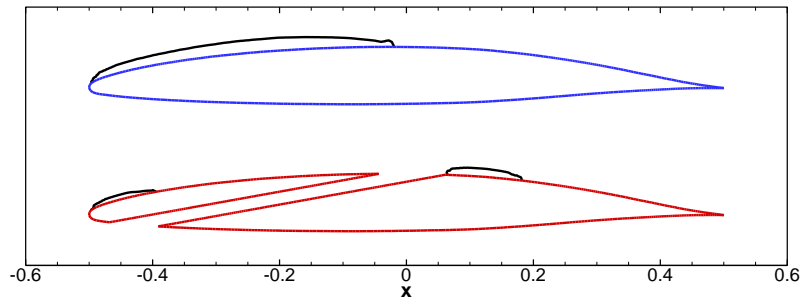


(b)

Fig. 16 The pressure (left column) and density (right column) contours for a) the original hydrofoil and for b) the optimized slotted hydrofoil.



(a)



(b)

Fig. 17 a) pressure coefficient distribution over the hydrofoil surfaces and b) their corresponding shape and the cavity pocket indicated by $C_p = -\sigma$.

6. Conclusion

In this paper, a slotted hydrofoil is optimized to find out the slot location and the slot angle that results in maximizing the lift coefficient and minimizing the total length of the cavity. Through the optimization procedure, a computational fluid dynamic (CFD) solver is required to provide the lift coefficient and the total length of the cavity for the optimizer. For this aim, the Frink numerical method is newly developed here to discretize the spatial terms in the preconditioned Euler equations based on the artificial compressibility method. The artificial dissipation terms are added to these equations for stability reasons and a sensor is used to retain the solution accuracy in smooth regions. Moreover, source terms that model the cavitation process are also added to the equations. The optimizer is constructed using a surrogated model based on the deep ANN surrogate model and the genetic algorithm. The Latin Hypercube algorithm is used to generate initial sample points in the design space. The outcome of the optimization process is an optimized slotted NACA 66 (MOD) hydrofoil satisfying the cost functions defined. Some conclusions and remarks regarding the present work are as follows:

- The comparison between results obtained by the CFD solver and available experimental results shows that the Frink finite volume-based solver newly proposed and developed here can be effectively used for simulating cavitating flows and can be considered as an alternative for the other cavitating flow solvers.
- Regarding the original hydrofoil NACA 66 (MOD), one cavity pocket is formed on its suction side. However, in the slotted hydrofoil, two cavities will emerge on the hydrofoil surface, namely, the leading-edge and mid-chord cavities. Smaller leading-edge cavity size will be found around $\theta = 45^\circ$ and at high slot angles. In the case of the mid-chord cavity, higher slot angles should be used with a slot placed around the middle.
- From the results obtained it can be concluded that high slot angles very close to the leading edge desirably result in the small total length of the cavity L_c and high lift coefficient C_l .
- The deep ANN surrogated mode is examined against CFD results which shows a good agreement with an error lower than 4%, thus it can be reliably used in the genetic algorithm for optimizing purposes.
- Results obtained for the optimized slotted hydrofoil show that with a penalty of about 11.4% in the lift coefficient, it is possible to decrease the cavity size by about 58.4%.

- The contours for the lift coefficient, the total length of the cavity, the length of the leading-edge cavity, and the length of the mid-chord cavity obtained in this study can be used by engineers to figure out how deviation from the optimum point can affect the performance of their artifacts.

Acknowledgment

Mahya Hajihassanpour would like to thank Prof. Kazem Hejranfar and Dr. Amir Hossein Khodabakhsh for their technical advice.

References

- [1] C. Tropea, A. L. Yarin, and J. F. Foss, *Springer handbook of experimental fluid mechanics*, vol. 1. Springer, 2007.
- [2] C. S. Pant, Y. Delorme, and S. Frankel, ‘Accuracy assessment of rans predictions of active flow control for hydrofoil cavitation’, *Processes*, vol. 8, no. 6, p. 677, 2020.
- [3] C.-S. Lee, B.-K. Ahn, J.-M. Han, and J.-H. Kim, ‘Propeller tip vortex cavitation control and induced noise suppression by water injection’, *J. Mar. Sci. Technol.*, vol. 23, pp. 453–463, 2018.
- [4] M. G. De Giorgi, A. Ficarella, and D. Fontanarosa, ‘Active Control of Unsteady Cavitating Flows in Turbomachinery’, presented at the Turbo Expo: Power for Land, Sea, and Air, American Society of Mechanical Engineers, 2019, p. V02AT45A027.
- [5] W. Wang, Q. Zhang, T. Tang, S. Lu, Q. Yi, and X. Wang, ‘Numerical study of the impact of water injection holes arrangement on cavitation flow control’, *Sci. Prog.*, vol. 103, no. 1, p. 0036850419877742, 2020.
- [6] P. Akbarzadeh and E. Akbarzadeh, ‘Hydrodynamic characteristics of blowing and suction on sheet-cavitating flows around hydrofoils’, *Ocean Eng.*, vol. 114, pp. 25–36, 2016.
- [7] B. Che and D. Wu, ‘Study on vortex generators for control of attached cavitation’, presented at the Fluids Engineering Division Summer Meeting, American Society of Mechanical Engineers, 2017, p. V01AT03A026.
- [8] B. Che, N. Chu, L. Cao, S. J. Schmidt, D. Likhachev, and D. Wu, ‘Control effect of micro vortex generators on attached cavitation instability’, *Phys. Fluids*, vol. 31, no. 6, 2019.

- [9] Q. Wei, H. Chen, and R. Zhang, ‘Numerical research on the performances of slot hydrofoil’, *J. Hydrodyn.*, vol. 27, no. 1, pp. 105–111, 2015.
- [10] Z. Li, Z. Qian, and B. Ji, ‘Transient cavitating flow structure and acoustic analysis of a hydrofoil with whalelike wavy leading edge’, *Appl. Math. Model.*, vol. 85, pp. 60–88, 2020.
- [11] T. Capurso, M. Lorusso, S. Camporeale, B. Fortunato, and M. Torresi, ‘Implementation of a passive control system for limiting cavitation around hydrofoils’, presented at the IOP Conference Series: Earth and Environmental Science, IOP Publishing, 2019, p. 032025.
- [12] T. Capurso, G. Menchise, G. Caramia, S. Camporeale, B. Fortunato, and M. Torresi, ‘Investigation of a passive control system for limiting cavitation inside turbomachinery under different operating conditions’, *Energy Procedia*, vol. 148, pp. 416–423, 2018.
- [13] F. R. Conesa and R. P. Liem, ‘Numerical investigation of cavitation performance of slotted hydrofoil for amphibious aircraft’, *Struct Congr*, vol. 126, p. 18, 2018.
- [14] F. R. Conesa and R. P. Liem, ‘Slotted hydrofoil design optimization to minimize cavitation in amphibious aircraft application: A numerical simulation approach’, *Adv. Aircr. Spacecr. Sci.*, vol. 7, no. 4, p. 309, 2020.
- [15] Z. Ni, M. Dhanak, and T. Su, ‘Performance of a slotted hydrofoil operating close to a free surface over a range of angles of attack’, *Ocean Eng.*, vol. 188, p. 106296, 2019.
- [16] E. Kadivar, O. el Moctar, and K. Javadi, ‘Stabilization of cloud cavitation instabilities using cylindrical cavitating-bubble generators (CCGs)’, *Int. J. Multiph. Flow*, vol. 115, pp. 108–125, 2019.
- [17] E. Amromin, ‘Design approach for cavitation tolerant hydrofoils and blades’, *J. Fluids Struct.*, vol. 45, pp. 96–106, 2014.
- [18] Q. Chen, Y. Liu, Q. Wu, Y. Wang, T. Liu, and G. Wang, ‘Global cavitation patterns and corresponding hydrodynamics of the hydrofoil with leading edge roughness’, *Acta Mech. Sin.*, vol. 36, pp. 1202–1214, 2020.
- [19] A. Ducoin, Y. L. Young, and J.-F. ois Sigrist, ‘Hydroelastic responses of a flexible hydrofoil in turbulent, cavitating flow’, presented at the Fluids Engineering Division Summer Meeting, 2010, pp. 493–502.
- [20] G. G. Wang and S. Shan, ‘Review of metamodeling techniques in support of engineering design optimization’, presented at the International Design Engineering Technical Conferences and Computers and Information in Engineering Conference, 2006, pp. 415–426.
- [21] J. P. Kleijnen, ‘Kriging metamodeling in simulation: A review’, *Eur. J. Oper. Res.*, vol. 192, no. 3, pp. 707–716, 2009.
- [22] A. Serani *et al.*, ‘Adaptive multi-fidelity sampling for CFD-based optimisation via radial basis function metamodels’, *Int. J. Comput. Fluid Dyn.*, vol. 33, no. 6–7, pp. 237–255, 2019.

- [23]J. Qian, J. Yi, Y. Cheng, J. Liu, and Q. Zhou, ‘A sequential constraints updating approach for Kriging surrogate model-assisted engineering optimization design problem’, *Eng. Comput.*, vol. 36, pp. 993–1009, 2020.
- [24]P. M. Zadeh, V. V. Toropov, and A. S. Wood, ‘Metamodel-based collaborative optimization framework’, *Struct. Multidiscip. Optim.*, vol. 38, pp. 103–115, 2009.
- [25]G. Li, V. Aute, and S. Azarm, ‘An accumulative error based adaptive design of experiments for offline metamodeling’, *Struct. Multidiscip. Optim.*, vol. 40, pp. 137–155, 2010.
- [26]D. Simon, *Evolutionary optimization algorithms*. John Wiley & Sons, 2013.
- [27]A. Gogna and A. Tayal, ‘Metaheuristics: review and application’, *J. Exp. Theor. Artif. Intell.*, vol. 25, no. 4, pp. 503–526, 2013.
- [28]M. Mitchell, ‘An introduction to genetic algorithms mit press’, *Camb. Mass. Lond. Engl.*, vol. 1996, 1996.
- [29]A. Kubota, H. Kato, and H. Yamaguchi, ‘A new modelling of cavitating flows: a numerical study of unsteady cavitation on a hydrofoil section’, *J. Fluid Mech.*, vol. 240, pp. 59–96, 1992.
- [30]J. H. Seo, Y. J. Moon, and B. R. Shin, ‘Prediction of cavitating flow noise by direct numerical simulation’, *J. Comput. Phys.*, vol. 227, no. 13, pp. 6511–6531, 2008.
- [31]J. Zheng, B. Khoo, and Z. Hu, ‘Simulation of wave-flow-cavitation interaction using a compressible homogenous flow method’, *Commun. Comput. Phys.*, vol. 14, no. 2, pp. 328–354, 2013.
- [32]Y. Chen, X. Chen, Z. Gong, J. Li, and C. Lu, ‘Numerical investigation on the dynamic behavior of sheet/cloud cavitation regimes around hydrofoil’, *Appl. Math. Model.*, vol. 40, no. 11–12, pp. 5835–5857, 2016.
- [33]M. Dumbser, U. Iben, and C.-D. Munz, ‘Efficient implementation of high order unstructured WENO schemes for cavitating flows’, *Comput. Fluids*, vol. 86, pp. 141–168, 2013.
- [34]F. Örley, V. Pasquariello, S. Hickel, and N. A. Adams, ‘Cut-element based immersed boundary method for moving geometries in compressible liquid flows with cavitation’, *J. Comput. Phys.*, vol. 283, pp. 1–22, 2015.
- [35]T. Uchiyama, ‘Numerical simulation of cavitating flow using the upstream finite element method’, *Appl. Math. Model.*, vol. 22, no. 4–5, pp. 235–250, 1998.
- [36]M. Hajihassanpour and K. Hejranfar, ‘A high-order nodal discontinuous Galerkin method to solve preconditioned multiphase Euler/Navier-Stokes equations for inviscid/viscous cavitating flows’, *Int. J. Numer. Methods Fluids*, vol. 92, no. 5, pp. 478–508, 2020.
- [37]K. Hejranfar and M. Hajihassanpour, ‘A high-order nodal discontinuous Galerkin method for solution of compressible non-cavitating and cavitating flows’, *Comput. Fluids*, vol. 156, pp. 175–199, 2017.

- [38]M. Hajihassanpour and K. Hejranfar, ‘A high-order nodal discontinuous Galerkin method for simulation of three-dimensional non-cavitating/cavitating flows’, *Finite Elem. Anal. Des.*, vol. 200, p. 103681, Mar. 2022, doi: 10.1016/j.finel.2021.103681.
- [39]N. Frink, ‘Recent progress toward a three-dimensional unstructured Navier-Stokes flow solver’, presented at the 32nd Aerospace Sciences Meeting and Exhibit, 1994, p. 61.
- [40]A. Jameson, W. Schmidt, and E. Turkel, ‘Numerical solution of the Euler equations by finite volume methods using Runge Kutta time stepping schemes’, presented at the 14th fluid and plasma dynamics conference, 1981, p. 1259.
- [41]M. Hajihassanpour and K. Hejranfar, ‘An implicit dual-time stepping high-order nodal discontinuous Galerkin method for solving incompressible flows on triangle elements’, *Math. Comput. Simul.*, vol. 168, pp. 173–214, 2020.
- [42]C. Markle, ‘Computational modeling of the dynamics of sheet cavitation’, presented at the Proc. 3rd International Symposium on Cavitation, 1998, pp. 307–311.
- [43]R. F. Kunz *et al.*, ‘A preconditioned Navier–Stokes method for two-phase flows with application to cavitation prediction’, *Comput. Fluids*, vol. 29, no. 8, pp. 849–875, 2000.
- [44]I. Senocak and W. Shyy, ‘Interfacial dynamics-based modelling of turbulent cavitating flows, Part-1: Model development and steady-state computations’, *Int. J. Numer. Methods Fluids*, vol. 44, no. 9, pp. 975–995, Mar. 2004, doi: 10.1002/flid.692.
- [45]A. SINGHAL, ‘Multi-dimensional simulation of cavitating flows using a PDF model of phase change’, *Proc ASME FED Meet. Vanc. Can. 1997*, 1997, [Online]. Available: <https://cir.nii.ac.jp/crid/1571417125694081152>
- [46]Z. Philip J., G. Andrew G., and B. Thabel, ‘A two-phase flow model for predicting cavitation dynamics’, *Fifth Int. Conf. Multiph. Flow*, vol. 152, 2004.
- [47]K. Hejranfar, E. Ezzatneshan, and K. Fattah-Hesari, ‘A comparative study of two cavitation modeling strategies for simulation of inviscid cavitating flows’, *Ocean Eng.*, vol. 108, pp. 257–275, Nov. 2015, doi: 10.1016/j.oceaneng.2015.07.016.
- [48]Y. Shen and P. Dimotakis, ‘The influence of Surface Cavitation on Hydrodynamic Forces’, presented at the SNAME 22nd American Towing Tank Conference, Aug. 1989, p. D011S001R006. doi: 10.5957/ATTC-1989-006.